Comput Mech (2008) 41:457–472
DOI 10.1007/s00466-007-0192-8

REVIEW ARTICLE

A gradient smoothing method (GSM) with directional correction for solid mechanics problems

G. R. Liu · Jian Zhang · K. Y. Lam · Hua Li · G. Xu · Z. H. Zhong · G. Y. Li · X. Han

Received: 26 July 2006 / Accepted: 7 May 2007 / Published online: 12 June 2007

Abstract A novel gradient smoothing method (GSM) is proposed in this paper, in which a gradient smoothing together with a directional derivative technique is adopted to develop the first- and second-order derivative approximations for a node of interest by systematically computing weights for a set of field nodes surrounding. A simple collocation procedure is then applied to the governing strong-from of system equations at each node scattered in the problem domain using the approximated derivatives. In contrast with the conventional finite difference and generalized finite difference methods with topological restrictions, the GSM can be easily applied to arbitrarily irregular meshes for complex geometry. Several numerical examples are presented to demonstrate the computational accuracy and stability of the GSM for solid mechanics problems with regular and irregular nodes. The GSM is examined in detail by comparison with other established numerical approaches such as the finite element method, producing convincing results.

Keywords Numerical methods · Gradient smoothing method (GSM) · Meshfree method · Solid mechanics · Numerical analysis

G. R. Liu (✉) · J. Zhang
Centre for Advanced Computations in Engineering Science,
Department of Mechanical Engineering,
National University of Singapore,
10 Kent Ridge Crescent, Singapore 119260, Singapore
e-mail: mpeliugr@nus.edu.sg

G. R. Liu
Singapore-MIT Alliance (SMA), E4-04-10,
4 Engineering Drive 3, Singapore 117576, Singapore

K. Y. Lam · H. Li
School of Mechanical and Aerospace Engineering,
Nanyang Technological University, 50 Nanyang Avenue,
Singapore 639798, Singapore

G. Xu
Institute of High Performance Computing, 1 Science Park Road,
#01-01 The Capricorn Singapore Science Park II,
Singapore 117528, Singapore

Z. H. Zhong · G. Y. Li · X. Han
Key Laboratory of Advanced Technology for Vehicle Body Design
and Manufacture, Hunan University, Changsha 410082,
Peoples Republic of China

1 Introduction

The finite difference method (FDM) is one of classical numerical tools for a broad class of initial-value and boundary-value problems [1–5]. Rapid development of computer technology since the early 1960s has resulted in reevaluation of the conventional numerical methods and search for new ones. The researchers realized that the traditional FDM utilizes regular structured and orthogonal meshes either in global Cartesian space [6] or in local curvilinear space [7–10]. It is difficult for the analysis by the classical FDM to automatically discretize boundary conditions, especially in the case of arbitrarily shaped domains. However, recently the development of the FDM generalized for arbitrarily unstructured grids (GFDM) [11–14] clearly indicates its potential power, which is comparable with the finite element method (FEM). It is shown that the GFDM may not only become equally universal, versatile, and suitable to full automation as the FEM, but also it is even more convenient in some areas of applications [15]. Moreover, the GFDM falls into the wider class of so-called meshfree methods [16,17]. They have been under intensive development in the recent years as a powerful alternative to the FEM. Comprehensive reviews on the development of meshfree methods can be found in many open literature such as Refs. [18–21].

The GFDM is considered as the category of meshfree strong-form methods [22], which directly discretizes the governing equations. The early contributors to the GFDM include Jensen [23], Perrone and Kao [24] etc. Later other investigators extended and improved the early formulations, which include the weighted moving least squares approximation [25], a unified GFDM/FEM system [26], the generalized finite strip approach [27], the adaptive GFDM [28] and multigrid GFDM solution approach [29], of which the most robust was developed by Liszka and Orkisz [30–32]. However, due to practical reasons, as well as for the purpose of generation of well-conditioned finite difference schemes, implementations of such methods using arbitrary irregular grids may sometimes be required to satisfy certain requirements, e.g., regularity in subdomains with guaranteed smooth transition, mesh with varying element topology and distribution of nodes with topological restrictions. Also, to consider finite difference (FD) operator generation at a node, one of the star selection criteria used in these methods and considered the best one [33], termed the Voronoi neighborhood criterion, is relatively more complicated and more difficult to be implemented for practical use.

In this paper we present a gradient smoothing method (GSM) based on the strong form formulation as an alternative to the generalized finite difference method for solving solid mechanics problems. Gradient smoothing technique is utilized to construct first- and second-order derivative approximations by systematically computing weights for a set of nodal points surrounding an interest node. These computations can be easily performed in parallel and are independent of the complexity and topology of a mesh. The flexibility of the GSM makes use of existing meshes that have originally been created for finite difference or finite element methods. A directional derivative technique is adopted to acquire a favourable weight distribution for the discrete differential operators, which helps greatly in solving the resulting set of algebraic system equations more efficiently and accurately.

This paper is organized as follows. In Sect. 2, a gradient smoothing technique is briefly introduced. Section 3 gives theoretical formulation and convergence study of the GSM. Several numerical examples are presented in Sect. 4, and conclusions are drawn in Sect. 5.

2 Gradient smoothing

A two-dimensional elastostatic problem is governed by the following equilibrium equation in the domain Ω:

$$\sigma_{ij,j} + b_i = 0 \quad \text{in}\,\Omega \tag{1}$$

where σ_{ij} is the stress tensor and b_i is the body force. Boundary conditions are given as follows:

$$u_i = \bar{u}_i \quad \text{on}\,\Gamma_u \tag{2}$$

$$\sigma_{ij}n_j - t_i = 0 \quad \text{on}\,\Gamma_t \tag{3}$$

where $\bar{u}_i$ denotes the prescribed boundary displacement on Dirichlet boundary Γ_u; t_i is the traction on Neumann boundary Γ_t and n_i is the unit outward normal vector.

It is supposed here that the problem domain Ω can be discretized by triangular cells (elements) as shown in Fig. 1. There are M field nodes in the problem domain Ω. For the ith node, a smoothing domain Ω_i is generated by sequentially connecting the centroids with mid-edge points of surrounding triangular cells. Γ_i is the boundary of the smoothing cell Ω_i. There is no overlapping between any two smoothing cells. That is,

$$\Omega = \sum_{i=1}^{M} \Omega_i,\, \Omega_1 \cap \Omega_2 \cap \cdots \cap \Omega_M = \emptyset \tag{4}$$

For constructing the difference schemes, a smooth operation to the gradient of field function u is proposed as follows: [34–36],

$$\nabla^h u(\mathbf{x}_i) = \int\limits_{\Omega_i} \nabla^h u(\mathbf{x})\Phi(\mathbf{x} - \mathbf{x}_i)d\Omega_i \tag{5}$$

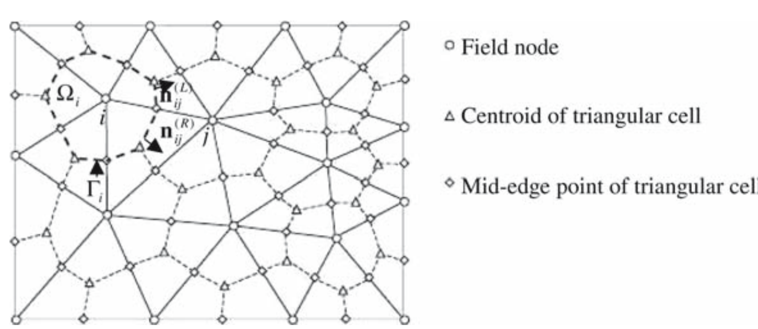

Fig. 1 Schematic of the triangular cells and smoothing cells created by sequentially connecting the centroids with mid-edge points of surrounding triangles for the ith node

Integration by parts for Eq. (5) leads to

$$\nabla^h u(\mathbf{x}_i) = \int_{\Gamma_i} u^h(\mathbf{x})\boldsymbol{n}(\mathbf{x})\Phi(\mathbf{x}-\mathbf{x}_i)d\Gamma - \int_{\Omega_i} u^h(\mathbf{x})\nabla\Phi(\mathbf{x}-\mathbf{x}_i)d\Omega \tag{6}$$

where Φ is a smoothing function.

Consider a weighted Shepard function [37] as the smoothing function

$$\Phi(\mathbf{x}-\mathbf{x}_i) = \frac{\phi(\mathbf{x}-\mathbf{x}_i)}{\sum_{j=1}^{M}\phi(\mathbf{x}-\mathbf{x}_j)A_j} \tag{7}$$

where $A_i = \int_{\Omega_i} d\Omega$ is the area (or volume) of the representative domain (smoothing domain) of the ith field node obtained from the diagram in Fig. 1. The weighted Shepard function in Eq. (7) meets the following weighted partition of unity:

$$\sum_{j=1}^{M}\Phi(\mathbf{x}-\mathbf{x}_j)A_j = 1 \tag{8}$$

For simplicity a piecewise constant function ϕ is given by

$$\phi(\mathbf{x}-\mathbf{x}_i) = \begin{cases} 1 & \mathbf{x}\in\Omega_i \\ 0 & \mathbf{x}\notin\Omega_i \end{cases} \tag{9}$$

Consequently the smoothing function is

$$\Phi(\mathbf{x}-\mathbf{x}_i) = \begin{cases} 1/A_i & \mathbf{x}\in\Omega_i \\ 0 & \mathbf{x}\notin\Omega_i \end{cases} \tag{10}$$

Substituting Eq. (10) into Eq. (6), the smoothed gradient of field function u is obtained:

$$\nabla^h u(\mathbf{x}_i) = \int_{\Gamma_i} u^h(\mathbf{x})\mathbf{n}(\mathbf{x})\Phi(\mathbf{x}-\mathbf{x}_i)d\Gamma = \frac{1}{A_i}\int_{\Gamma_i} u^h(\mathbf{x})\mathbf{n}(\mathbf{x})d\Gamma \tag{11}$$

Note that the choice of constant Φ makes the second term on the right-hand side of Eq. (6) vanish. The area integration becomes line integration along the edges of smoothing cell in Eq. (5). Equqtion (11) can be rewritten in the discrete form as

$$\nabla^h u_i = \frac{1}{A_i}\sum_{j=1}^{m_i}\left(L_{ij}^{(L)}\mathbf{n}_{ij}^{(L)}u_{ij}^{(L)} + L_{ij}^{(R)}\mathbf{n}_{ij}^{(R)}u_{ij}^{(R)}\right) \tag{12}$$

where m_i is the number of surrounding cells for the ith field node. As shown in Fig. 1, $L_{ij}^{(L)}$ and $L_{ij}^{(R)}$ are the lengths of two straight edges along the smoothing boundary located at the left- and right-hand sides of the edge $i-j$ respectively, $\mathbf{n}_{ij}^{(L)}$ and $\mathbf{n}_{ij}^{(R)}$ are the corresponding outward normal vectors, and $u_{ij}^{(L)}$ and $u_{ij}^{(R)}$ are the approximated field functions (e.g., displacements) along the two straight edges. Similarly, according to the procedures described in Eqs. (5)–(11), the second-order gradient of field function u can be evaluated easily by differentiating Eq. (11) as

$$\nabla^2 u(\mathbf{x}_i) = \frac{1}{A_i}\int_{\Gamma_i}\nabla^h u(\mathbf{x})\mathbf{n}(\mathbf{x})d\Gamma \tag{13}$$

To get the values of $u_{ij}^{(L)}$ and $u_{ij}^{(R)}$ in the Eq. (12), various schemes can be adopted. The details are to be introduced in the following section.

3 Gradient smoothing method (GSM)

In this section, the gradient smoothing method is formulated for the approximation of the derivatives that will be used in the simple collocation procedure to obtain a set of algebraic system equations. Different rules for constructing difference schemes are first introduced. A stability analysis is then conducted to reveal the accuracy of the GSM method. Finally, several numerical studies on computing accuracy and convergence are carried out using a Poisson's equation problem for both regularly and irregularly distributed meshes.

3.1 Formulation of different rules

3.1.1 Rectangular rule

As described in Sect. 2, the gradient of field function $u(x, y)$ at field node (x_i, y_i) can be approximated by line integrating along the closed edges of smoothing cell Ω_i. From Eq. (12), we have

$$\frac{\partial u_i}{\partial x} = \frac{1}{A_i}\sum_{j=1}^{m_i}\frac{1}{2}\Delta LX_{ij}(u_i + u_{(j)}) \tag{14}$$

$$\frac{\partial u_i}{\partial y} = \frac{1}{A_i}\sum_{j=1}^{m_i}\frac{1}{2}\Delta LY_{ij}(u_i + u_{(j)}) \tag{15}$$

with

$$\Delta LX_{ij} = \Delta LX_{ij}^{(L)} + \Delta LX_{ij}^{(R)} = L_{ij}^{(L)}n_x^{(L)} + L_{ij}^{(R)}n_x^{(R)} \tag{16}$$

$$\Delta LY_{ij} = \Delta LY_{ij}^{(L)} + \Delta LY_{ij}^{(R)} = L_{ij}^{(L)}n_y^{(L)} + L_{ij}^{(R)}n_y^{(R)} \tag{17}$$

where $n_x^{(L)}, n_y^{(L)}, n_x^{(R)}$ and $n_y^{(R)}$ are the components of the unit outward normal vectors in x- and y-directions on the two edges located at the left- and right-hand sides of the edge $i-j$, respectively. $u_{(j)}$ denotes the value of field function u at the jth $(j = 1, 2, \ldots, m_i)$ surrounding node of the ith field node. Note that the numbering of j is counterclockwise in this paper.

Similarly, the second-order derivatives can be expressed as

$$\frac{\partial^2 u_i}{\partial x^2} = \frac{1}{A_i}\sum_{j=1}^{m_i}\frac{1}{2}\Delta LX_{ij}\left(\frac{\partial u_i}{\partial x}+\frac{\partial u_{(j)}}{\partial x}\right) \tag{18}$$

$$\frac{\partial^2 u_i}{\partial y^2} = \frac{1}{A_i}\sum_{j=1}^{m_i}\frac{1}{2}\Delta LY_{ij}\left(\frac{\partial u_i}{\partial y}+\frac{\partial u_{(j)}}{\partial y}\right) \tag{19}$$

$$\frac{\partial^2 u_i}{\partial x\partial y} = \frac{1}{A_i}\sum_{j=1}^{m_i}\frac{1}{2}\Delta LY_{ij}\left(\frac{\partial u_i}{\partial x}+\frac{\partial u_{(j)}}{\partial x}\right) \tag{20}$$

The formulation in Eqs. (14)–(20) is based on rectangular rule, where function values along the two straight edges located at the left- and right-hand sides of the edge $i-j$ are approximated only according to the mid-edge points of the surrounding cells for the ith field node. Thus, by arithmetically averaging function values at the both edge ends, the values at mid-edge points can be obtained easily. The centroids of surrounding cells contribute only to the geometrical calculations of ΔLX_{ij} and ΔLY_{ij}.

3.1.2 Trapezoidal rule

The present trapezoidal rule is different from the above rectangular one, and it evaluates the function values along the two straight edges located at the left- and right-hand sides of the edge $i-j$ according to both the mid-edge points and centroids of surrounding cells. Function values and gradients at mid-edge points are evaluated by arithmetically averaging those at the both edge ends. At centroids, they are obtained with arithmetically averaging values at vertices composing of the surrounding cells.

From Eq. (12), the following expressions can be obtained

$$\frac{\partial u_i}{\partial x} = \frac{1}{A_i}\sum_{j=1}^{m_i}\left[\frac{1}{2}\Delta LX_{ij}^{(L)}\left(u_m+u_c^{(L)}\right)\right.$$
$$\left.+\frac{1}{2}\Delta LX_{ij}^{(R)}\left(u_m+u_c^{(R)}\right)\right] \tag{21}$$

$$\frac{\partial u_i}{\partial y} = \frac{1}{A_i}\sum_{j=1}^{m_i}\left[\frac{1}{2}\Delta LY_{ij}^{(L)}\left(u_m+u_c^{(L)}\right)\right.$$
$$\left.+\frac{1}{2}\Delta LY_{ij}^{(R)}\left(u_m+u_c^{(R)}\right)\right] \tag{22}$$

where

$$u_m = (u_i + u_{(j)})/2 \tag{23}$$

$$u_c^{(L)} = (u_i + u_{(j)} + u_{(j+1)})/3 \tag{24}$$

$$u_c^{(R)} = \begin{cases} (u_i + u_{(j)} + u_{(j-1)})/3 & j = 2, 3, \ldots, m_i \\ (u_i + u_{(1)} + u_{(m_i)})/3 & j = 1 \end{cases} \tag{25}$$

The second-order derivatives by the trapezoidal rule are

$$\frac{\partial^2 u_i}{\partial x^2} = \frac{1}{A_i}\sum_{j=1}^{m_i}\left[\frac{1}{2}\Delta LX_{ij}^{(L)}\left(\frac{\partial u_m}{\partial x}+\frac{\partial u_c^{(L)}}{\partial x}\right)\right.$$
$$\left.+\frac{1}{2}\Delta LX_{ij}^{(R)}\left(\frac{\partial u_m}{\partial x}+\frac{\partial u_c^{(R)}}{\partial x}\right)\right] \tag{26}$$

$$\frac{\partial^2 u_i}{\partial y^2} = \frac{1}{A_i}\sum_{j=1}^{m_i}\left[\frac{1}{2}\Delta LY_{ij}^{(L)}\left(\frac{\partial u_m}{\partial y}+\frac{\partial u_c^{(L)}}{\partial y}\right)\right.$$
$$\left.+\frac{1}{2}\Delta LY_{ij}^{(R)}\left(\frac{\partial u_m}{\partial y}+\frac{\partial u_c^{(R)}}{\partial y}\right)\right] \tag{27}$$

$$\frac{\partial^2 u_i}{\partial x\partial y} = \frac{1}{A_i}\sum_{j=1}^{m_i}\left[\frac{1}{2}\Delta LY_{ij}^{(L)}\left(\frac{\partial u_m}{\partial x}+\frac{\partial u_c^{(L)}}{\partial x}\right)\right.$$
$$\left.+\frac{1}{2}\Delta LY_{ij}^{(R)}\left(\frac{\partial u_m}{\partial x}+\frac{\partial u_c^{(R)}}{\partial x}\right)\right] \tag{28}$$

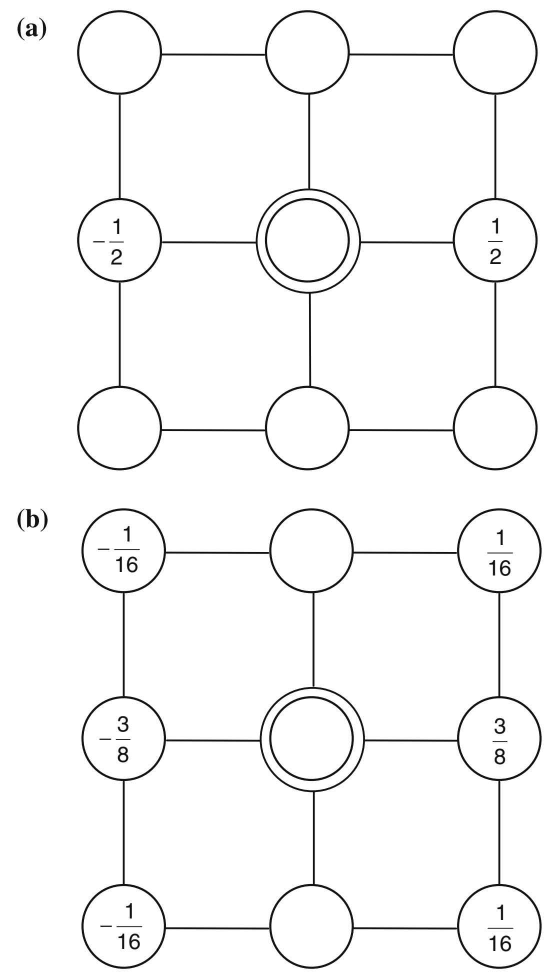

Fig. 2 GSM weights for operator ∇h in regular mesh: **a** rectangular rule; **b** trapezoidal rule

where

$$\nabla u_m = (\nabla u_i + \nabla u_{(j)})/2 \quad (29)$$

$$\nabla u_c^{(L)} = (\nabla u_i + \nabla u_{(j)} + \nabla u_{(j+1)})/3 \quad (30)$$

$$\nabla u_c^{(R)} = \begin{cases} (\nabla u_i + \nabla u_{(j)} + \nabla u_{(j-1)})/3 & j = 2, 3, \ldots, m_i \\ (\nabla u_i + \nabla u_{(1)} + \nabla u_{(m_i)})/3 & j = 1 \end{cases} \quad (31)$$

3.2 Stability analysis of the GSM

To investigate the property of the aforementioned different rules, an intensive numerical study is conducted from the regular (structured) meshes. Based on the rectangular and trapezoidal rules, several typical discrete differential operators generated on regular meshes are presented in Figs. 2 and 3, where the grid interval is h in both x- and y-directions. All of these only use the nodal values of the function, and do not include their derivatives. As shown in Fig. 3, both the rectangular and trapezoidal rules lead to wide stencils with unfavourable weight distributions for the Laplace operator $\nabla^2 h^2$. It was demonstrated [38] that the stencils allow the decoupling of the solution on quadrilateral grids.

The properties of both the rules can be improved, and particularly the decoupling effect can be prevented by the directional derivative along the edge $i - j$ (see Fig. 1), i.e.,

$$\left(\frac{\partial u}{\partial l}\right)_{ij} \approx \frac{u_{(j)} - u_i}{l_{ij}} \quad (32)$$

where l_{ij} represents the distance between the ith field node and its jth surrounding node. Denote the vector from the

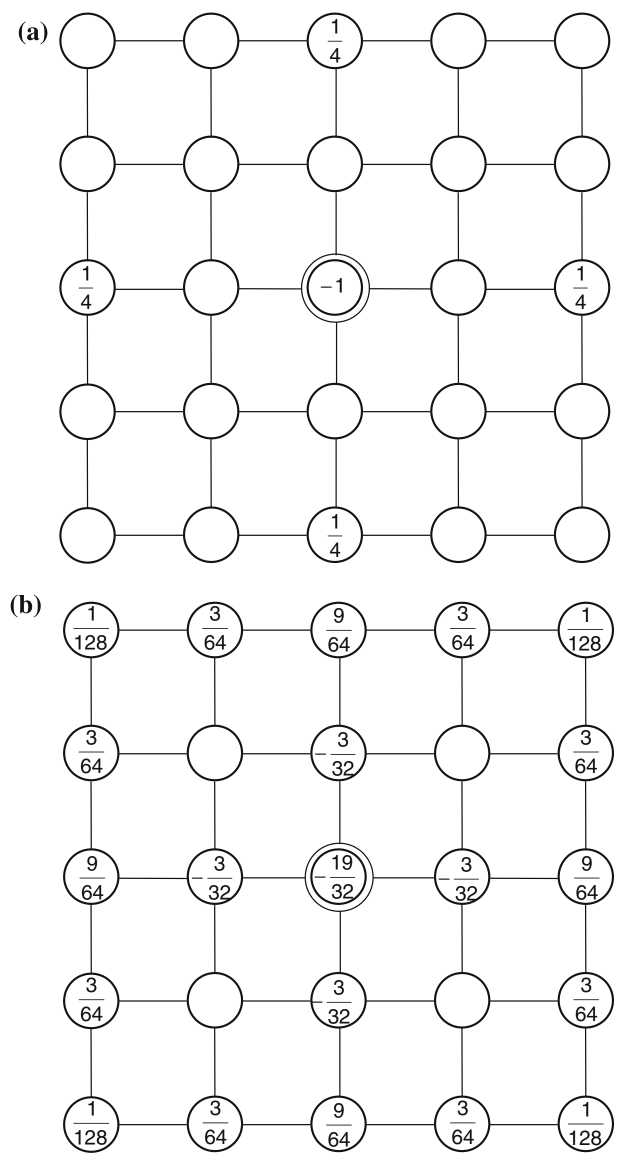

Fig. 3 GSM weights for $\nabla^2 h^2$ in regular mesh: **a** rectangular rule; **b** trapezoidal rule

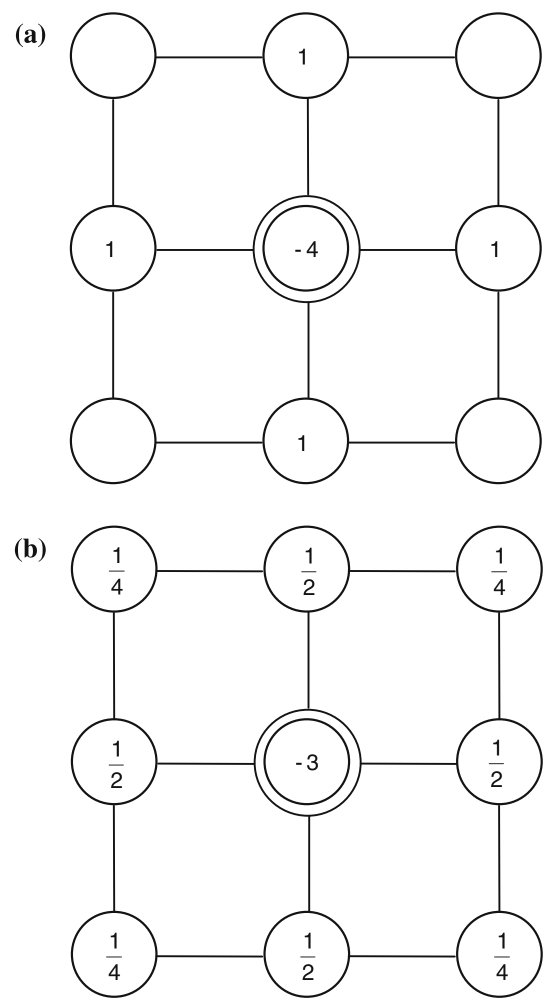

Fig. 4 GSM weights for operator $\nabla^2 h^2$ in regular mesh: **a** modified rectangular rule; **b** modified trapezoidal rule

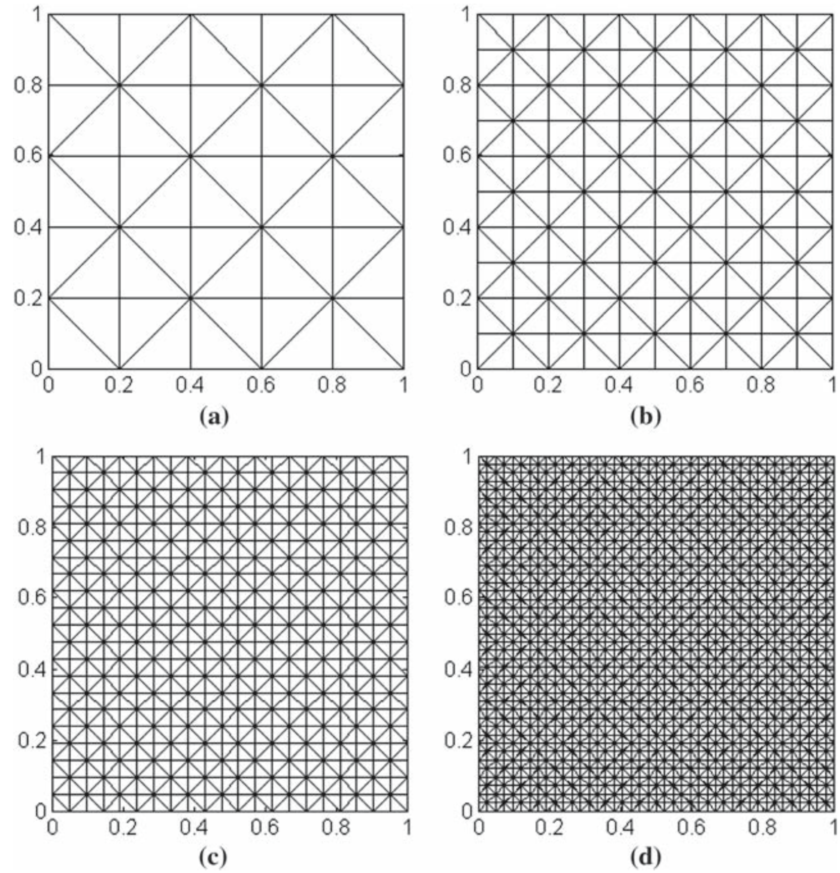

Fig. 5 Regular element distribution of Poisson's equation: **a** 50; **b** 200; **c** 882; **d** 3,528 elements

Table 1 Comparison of error norms (e_u) of Poisson's equation with Dirichlet boundary conditions for regularly distributed nodes computed using different rules

No. of field nodes	36	121	484	1849
Rectangular rule	0.26729	6.2094E−2	1.3954E−2	3.5096E−3
Trapezoidal rule	0.26729	6.2094E−2	1.3954E−2	3.5096E−3
Rectangular (modified)	6.6548E−2	1.6491E−2	3.7322E−3	9.3269E−4
Trapezoidal (modified)	5.2167E−2	1.2647E−2	2.8468E−3	7.1060E−4

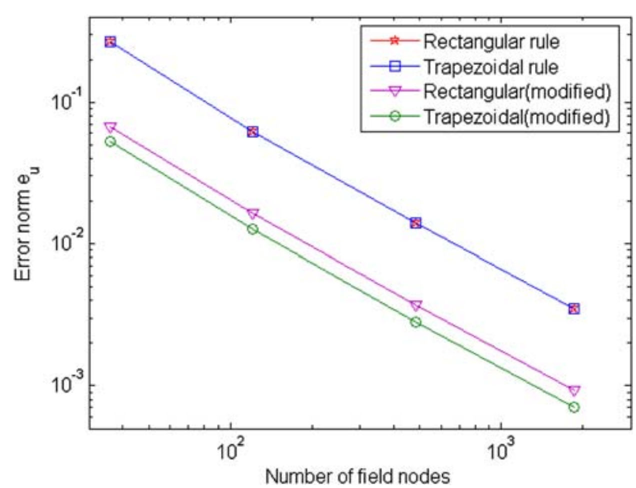

Fig. 6 Comparison of error norms of Poisson's equation with Dirichlet boundary conditions for regularly distributed nodes computed using different rules

node i to its jth surrounding node as

$$\vec{r}_{ij} = \vec{r}_j - \vec{r}_i \tag{33}$$

With the definition of the unit vector $\vec{t}_{ij}$ along the line connecting the node i and its jth surrounding node,

$$\vec{t}_{ij} = \frac{\vec{r}_{ij}}{l_{ij}} \tag{34}$$

the modified average gradient may be written as [39,40]

$$\nabla u_{ij} = \nabla \vec{u}_{ij} - \left[\nabla \vec{u}_{ij} \cdot \vec{t}_{ij} - \left(\frac{\partial u}{\partial l} \right)_{ij} \right] \vec{t}_{ij} \tag{35}$$

where $\nabla\vec{u}_{ij}$ is given by

$$\nabla\vec{u}_{ij} = \frac{1}{2}(\nabla\vec{u}_i + \nabla\vec{u}_{(j)}) \quad (36)$$

The modification leads to strongly coupled stencils on quadrilateral as well as on triangular grids [38].

The above modified average gradient in Eq. (35) uses the directional derivative along the edge connecting the node i and its jth surrounding node, which is applicable to both the rectangular and trapezoidal rules described in Sects. 3.1.1 and 3.1.1. A modified rectangular rule is obtained after incorporating this technique into the former rectangular rule. As for the trapezoidal rule, both the modified average gradient along the cell edge and the cell-based gradient by applying Green–Gauss theorem are adopted to generate the modified trapezoidal rule. Namely, function values at the centroids of surrounding cells for the node i are obtained with arithmetic averaging of values at vertices of the surrounding cells, and relevant gradients are approximated by applying Green-Gauss theorem on the cell-based gradient smoothing domain. This modified trapezoidal rule is the presently proposed novel gradient smoothing method (GSM) for all the investigations in this paper.

Using the modified rectangular and trapezoidal rules, the typical Laplace operator $\nabla^2 h^2$ based on structured grids can be obtained and shown as in Fig. 4. Applied to the regular grids, the modification to the rectangular rule is nothing but central-differencing for midpoints of the grids. That is, the modified rectangular rule has the property of consistency with the classic finite difference. As shown in Fig. 4b, the modified trapezoidal rule (GSM) generates a stencil with a favourable weight distribution for the Laplace operator $\nabla^2 h^2$. Thus, the GSM is consistent to the partial differential equations, which will guarantee the stability of the solution.

3.3 Convergence study of the GSM

In this study, the proposed GSM is first examined through solving a two-dimensional Poisson's equation as

$$\frac{\partial^2 u}{\partial x^2} + \frac{\partial^2 u}{\partial y^2} = \sin(\pi x)\sin(\pi y) \quad (37)$$

with problem domain $\Omega = \{(x, y) \in [0,\ 1;\ 0,\ 1]\}$. The corresponding exact solution is

$$u(x, y) = -\frac{1}{2\pi^2}\sin(\pi x)\sin(\pi y) \quad (38)$$

Dirichlet and Neumann boundary conditions are considered for regularly and irregularly distributed nodes, respectively. In the numerical studies, a norm as an error indicator is defined as

$$e_u = \sqrt{\frac{\sum\left(u^{\text{numerical}} - u^{\text{exact}}\right)^2}{\sum\left(u^{\text{exact}}\right)^2}} \quad (39)$$

Table 2 Relative errors of Poisson's equation with Dirichlet boundary conditions computed using the same sets of regularly distributed nodes for GSM and FEM

No. of field nodes	36	121	484	1849
h	0.2	0.1	0.0476	0.0238
e_u				
GSM	5.2167E−2	1.2647E−2	2.8468E−3	7.1060E−4
FEM	4.6600E−2	1.1600E−2	2.6000E−3	6.5940E−4
$e_{\partial u/\partial x}$				
GSM	0.20343	7.7494E−2	2.3482E−2	8.4210E−3
FEM	0.22220	8.1900E−2	2.4400E−2	8.6000E−3

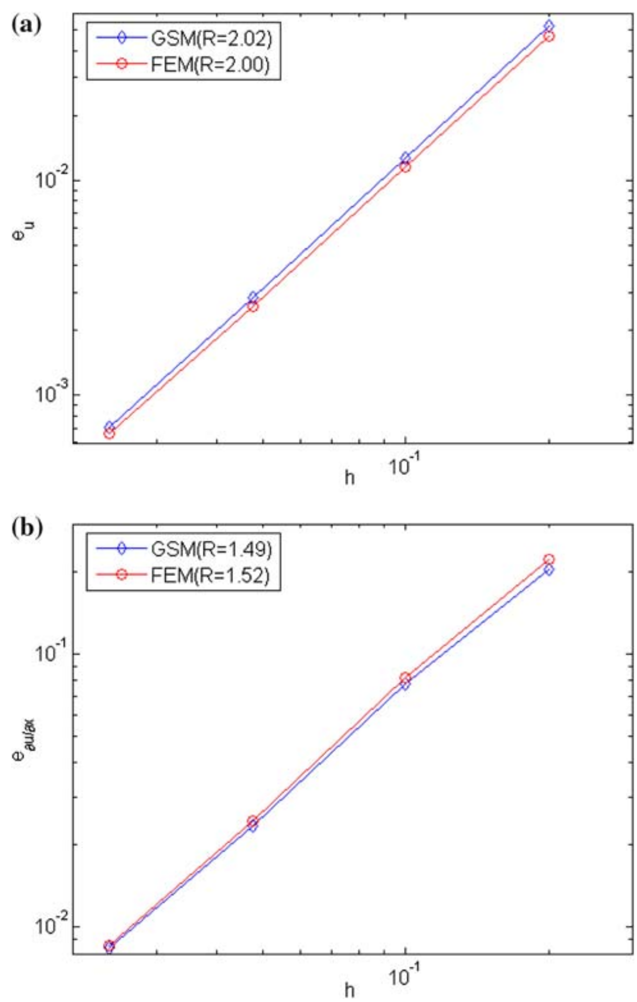

Fig. 7 Comparison of convergence rate and accuracy between GSM and FEM for Poisson's equation with regular nodes: **a** Error norm e_u; **b** Error norm $e_{\partial u/\partial x}$

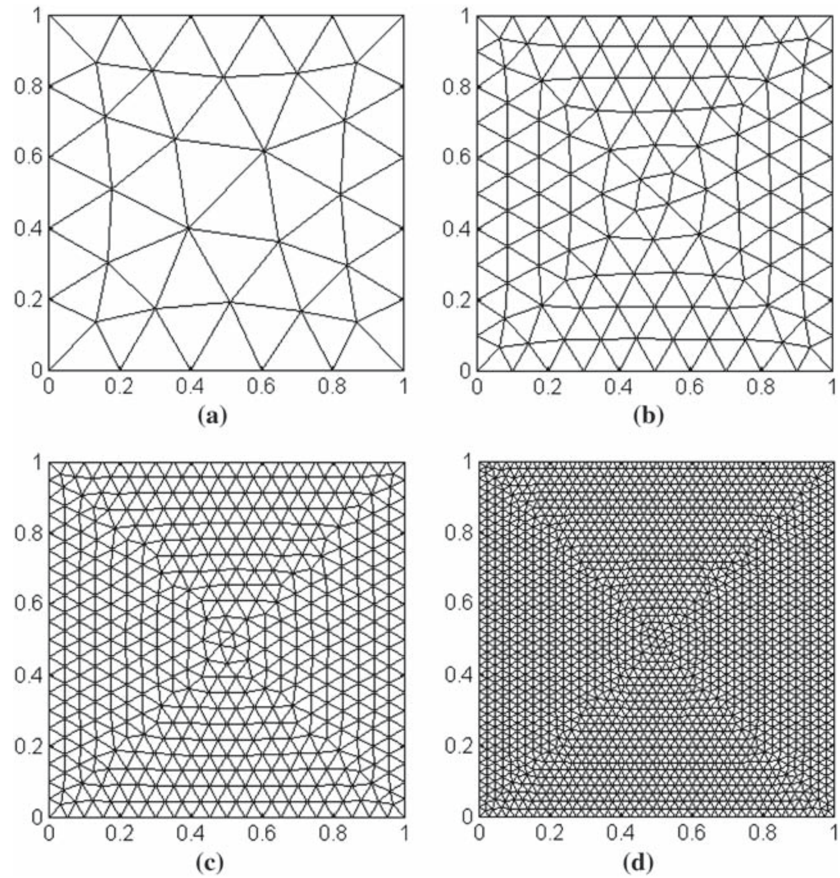

Fig. 8 Irregular element distribution of Poisson's equation: **a** 58; **b** 222; **c** 894; **d** 3,632 elements

Table 3 Comparison of error norms (e_u) of Poisson's equation with Neumann boundary conditions for irregularly distributed nodes computed using different rules

No. of field nodes	40	132	488	1897
Rectangular rule	0.28030	6.5462E−2	1.5997E−2	3.9955E−3
Trapezoidal rule	0.27425	6.5180E−2	1.5665E−2	3.8869E−3
Rectangular (modified)	8.2456E−2	1.5604E−2	3.0192E−3	6.2920E−4
Trapezoidal (modified)	6.7903E−2	1.3605E−2	2.7761E−3	6.0463E−4

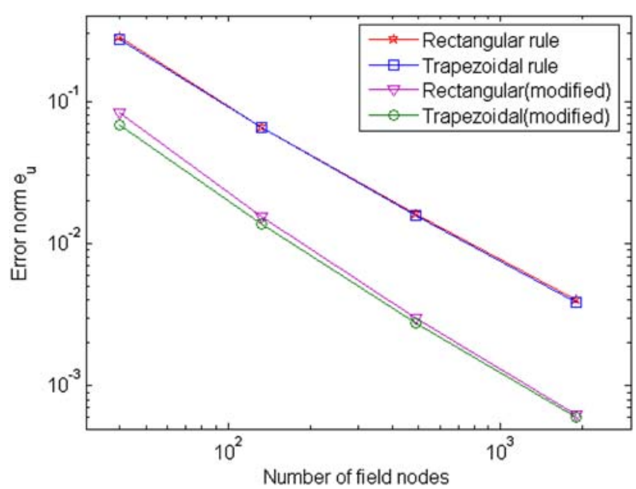

Fig. 9 Comparison of error norms of Poisson's equation with Neumann boundary conditions for irregularly distributed nodes computed using different rules

Similarly, the error norm for the first-order derivative is

$$e_{\partial u/\partial x} = \sqrt{\frac{\sum\left[\left(\frac{\partial u}{\partial x}\right)^{\text{numerical}} - \left(\frac{\partial u}{\partial x}\right)^{\text{exact}}\right]^2}{\sum\left[\left(\frac{\partial u}{\partial x}\right)^{\text{exact}}\right]^2}} \tag{40}$$

We start with the four regular distributions of 6×6, 11×11, 22×22 and 43×43 field nodes, as shown in Fig. 5. A Dirichlet boundary is considered, in which the essential boundary conditions are imposed on all edges as

$$u = 0 \quad \text{along}\, x = 0,\ x = 1,\ y = 0 \quad \text{and} \quad y = 1 \tag{41}$$

The overall error norms of the field variable u for the various rules discussed in Sects. 3.1 and 3.2 are shown in Table 1 and Fig. 6. Compared with the other rules, the GSM (modified trapezoidal rule) achieves the best linear steady convergence. The relative errors in u and $\frac{\partial u}{\partial x}$ of GSM are compared with three-node linear finite elements in Table 2 and Fig. 7. The convergence rates are also demonstrated in Fig. 7, where h is the averaged element size. As shown in Fig. 7a, the GSM achieves a little higher convergence rate for field variable u compared with the linear FEM. As for the first-order derivative $\frac{\partial u}{\partial x}$ in Fig. 7b, the GSM is more accurate than FEM.

Further, the four distributions of irregular field nodes presented in Fig. 8 are investigated. They are 40, 132, 488 and 1,897 nodes, respectively. The mixed boundary conditions are considered here in problem domain Ω, where Neumann boundary conditions are

$$\left.\frac{\partial u}{\partial x}\right|_{x=0} = -\frac{1}{2\pi}\sin(\pi y), \quad \left.\frac{\partial u}{\partial x}\right|_{x=1} = \frac{1}{2\pi}\sin(\pi y) \tag{42}$$

and Dirichlet boundary conditions are

$$u = 0 \quad \text{along } y = 0 \text{ and } y = 1 \tag{43}$$

The overall error norm of field variable u using the GSM has been much improved from 6.79 to 0.06%, as shown in Table 3 and Fig. 9. The relative errors in u and $\frac{\partial u}{\partial x}$ for GSM and FEM are presented in Table 4 and Fig. 10. As shown in Fig. 10a, the GSM not only achieves a higher convergence rate but also obtains more accurate results than FEM. With the increase of irregular nodes, it appears that GSM are more and more accurate than FEM. Similarly, it can be seen from Fig. 10b that the GSM is more accurate than FEM in the computation of the first-order derivatives of variable u. This is because the GSM directly discretizes the governing equations based on the gradient smoothing technique which guarantees the first-order continuity. However, in terms of the first-order derivatives (e.g., stresses and strains), the FEM suffers from discontinuity problems and requires the use of post processing to produce better results.

Table 4 Relative errors of Poisson's equation with Neumann boundary conditions computed using the same sets of irregularly distributed nodes for GSM and FEM

No. of field nodes	40	132	488	1897
h	0.1878	0.09534	0.04741	0.02350
e_u				
GSM	6.7903E−2	1.3605E−2	2.7761E−3	6.0463E−4
FEM	6.7900E−2	1.4800E−2	3.3000E−3	7.7356E−4
$e_{\partial u/\partial x}$				
GSM	0.15545	5.3777E−2	1.9578E−2	6.8747E−3
FEM	0.1881	6.4200E−2	2.1700E−2	7.2000E−3

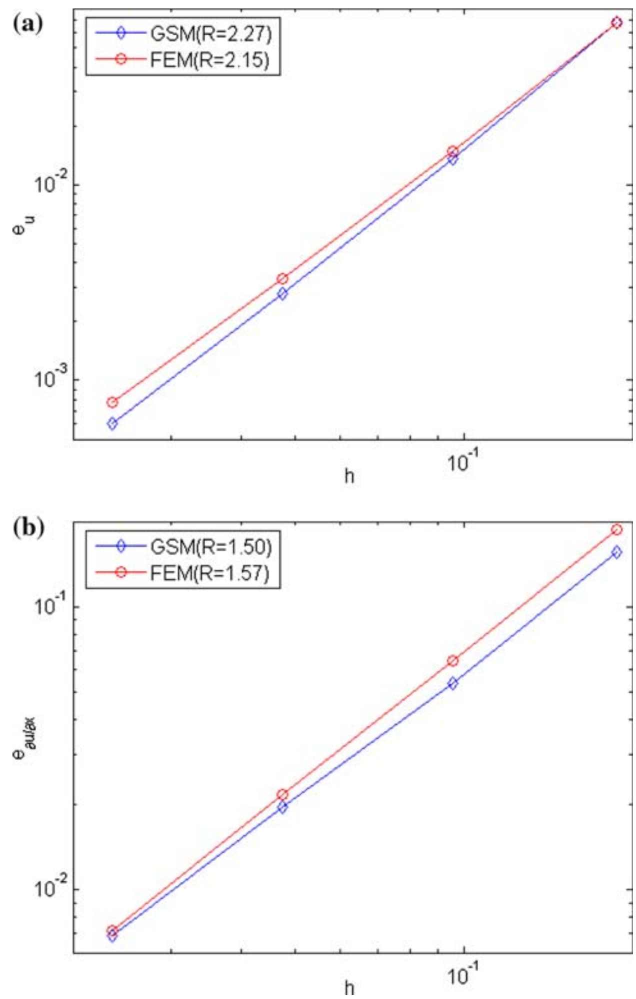

Fig. 10 Comparison of convergence rate and accuracy between GSM and FEM for Poisson's equation with irregular nodes: **a** Error norm e_u; **b** Error norm $e_{\partial u/\partial x}$

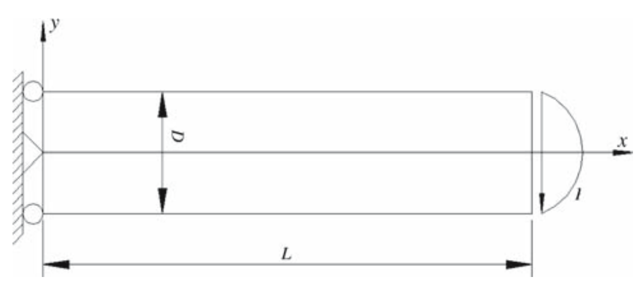

Fig. 11 Cantilever beam subjected to a parabolic load at the free end

It can be observed from this numerical study that the GSM is quite stable even with the Neumann boundary conditions and yields very accurate results for both the regular and irregular field node distributions.

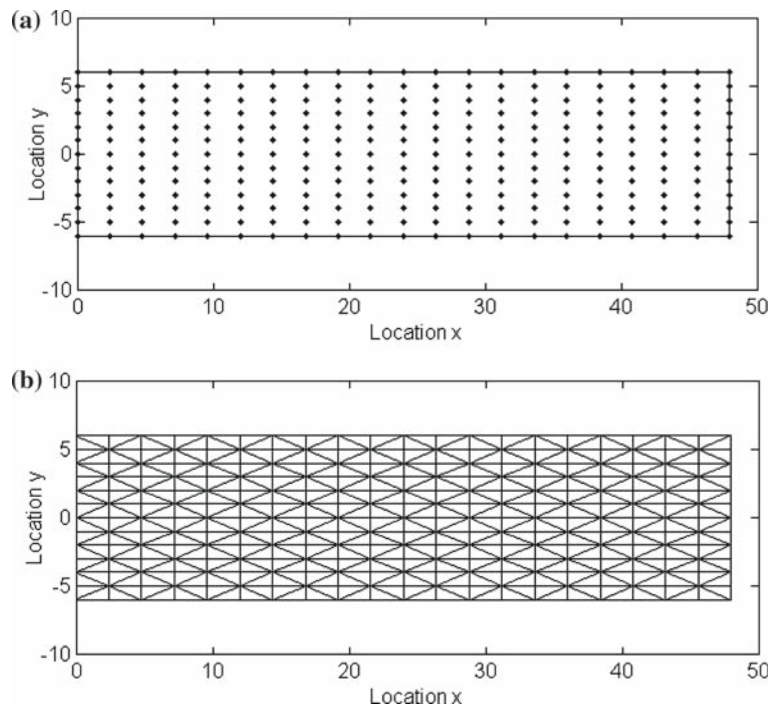

Fig. 12 Domain discretization of cantilever beam: **a** node distribution; **b** element distribution

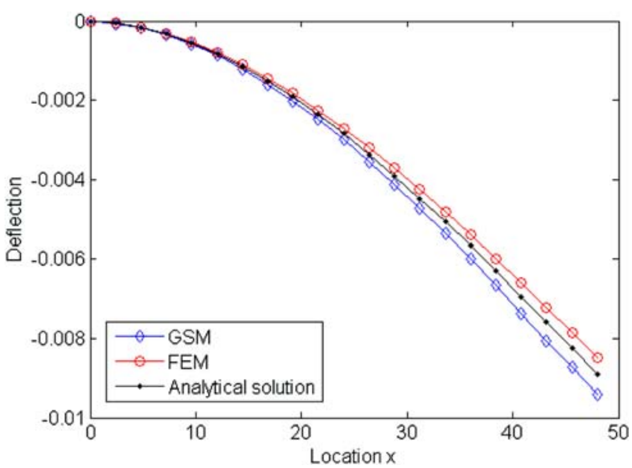

Fig. 13 Deflection of cantilever beam along the line $y = 0$ computed using the same mesh (480 triangular elements) for GSM and FEM

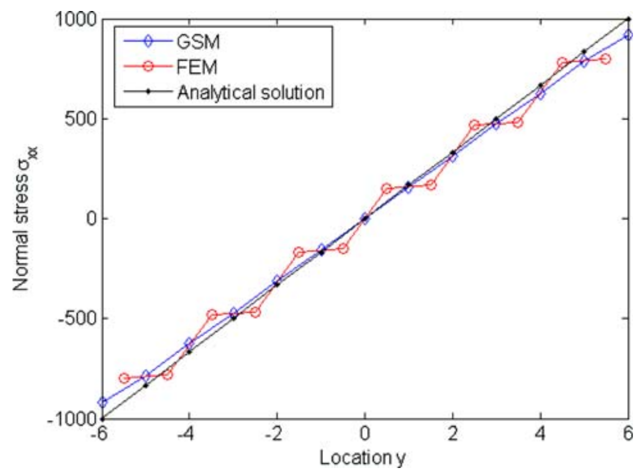

Fig. 14 Normal stress σ_{xx} along the line $x = L/2$ computed using the same mesh (480 triangular elements) for GSM and FEM

4 Numerical examples

4.1 Cantilever beam

A 2-D cantilever beam with length L and height D subjected to a parabolic traction at the free end is studied as a benchmark problem here, as shown in Fig. 11. Assume the beam has a unit thickness so that the problem is simplified into plane stress case. The analytical solution is available by Timoshenko and Goodier [41]:

$$u_x = -\frac{Py}{6EI}\left[(6L-3x)x+(2+\nu)\left(y^2-\frac{D^2}{4}\right)\right] \tag{44}$$

$$u_y = \frac{P}{6EI}\left[3\nu y^2(L-x)+(4+5\nu)\frac{D^2x}{4}+(3L-x)x^2\right] \tag{45}$$

$$\sigma_{xx} = -\frac{P(L-x)y}{I} \tag{46}$$

$$\sigma_{yy} = 0 \tag{47}$$

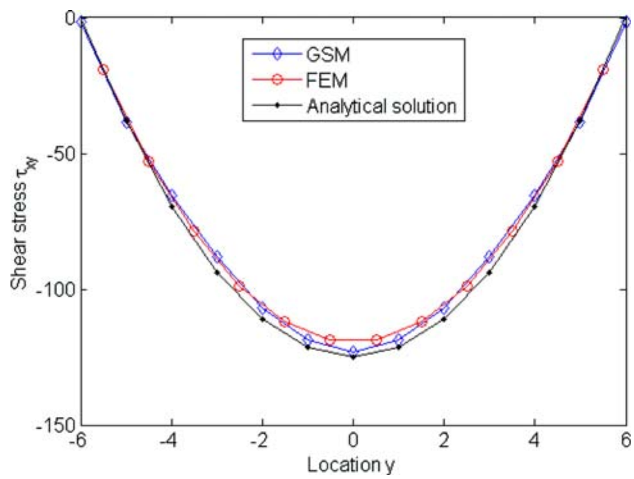

Fig. 15 Shear stress τ_{xy} along the line $x = L/2$ computed using the same mesh (480 triangular elements) for GSM and FEM

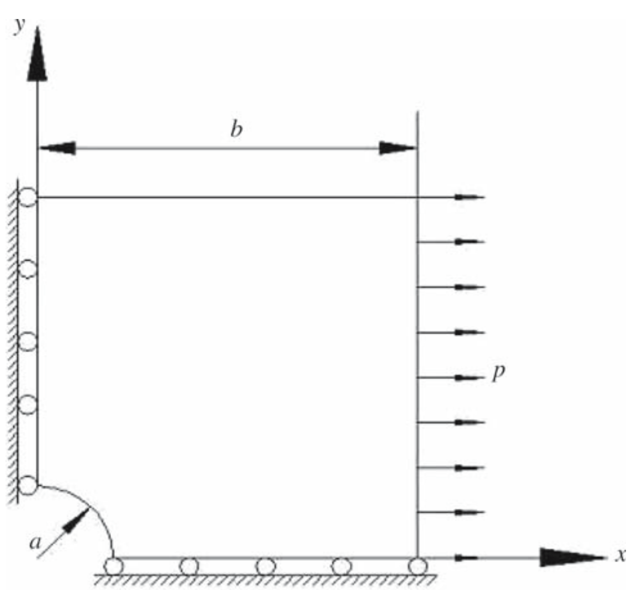

Fig. 16 Quarter model of the infinite plate with a circular hole subjected to a unidirectional tensile load

Table 5 Comparison of the CPU time computed using GSM and FEM

No. of field nodes	CPU time of GSM (s)	CPU time of FEM (s)
273	0.73	1.67
527	1.83	3.14
1127	5.67	6.53
2275	26.78	16.34
3825	84.76	44.25

$$\tau_{xy} = \frac{P}{2I}\left(\frac{D^2}{4} - y^2\right) \tag{48}$$

where the moment of inertia I for a beam with rectangular cross section and unit thickness is given by $I = D^3/12$. The geometries and material properties are taken as $L = 48$m, $D = 12$ m, Young's modulus $E = 3 \times 10^7$ N/m^2, Poisson's ratio $\nu = 0.3$, loading (integration of the distributed traction) $P = -1000$ N. The governing equations of this problem are given by Eqs. (1)–(3), which are also used for the following numerical investigations.

In this study, cantilever beam is simulated by 273 regularly distributed nodes and 480 triangular elements as shown in Fig. 12a and b. To validate the present method, the GSM results are compared with the FEM and analytical solutions, respectively. The same set of nodes and elements are used for modeling of cantilever beam by the GSM and FEM. In the FEM, three-node linear element and 3 gauss integration points are used in the numerical integration scheme.

The computing results of the deflection along the line $y = 0$ are plotted in Fig. 13. From this figure, it is observed that the GSM is able to provide the results as accurate as the FEM for deflection of the cantilever beam as shown in Fig. 13. In terms of stresses, the FEM requires post processing procedures to provide better results as it suffers from discontinuity in stresses. In contrast, the GSM does not encounter discontinuity problem in stresses. As shown in Fig. 14, the normal stress σ_{xx} computed by the GSM is smooth rather

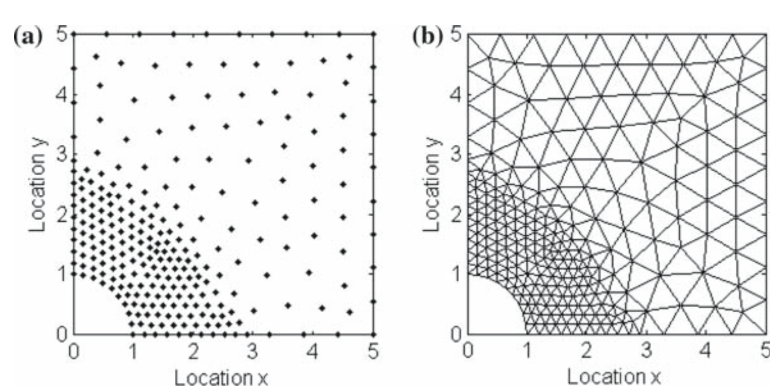

Fig. 17 Quarter model of the infinite plate: **a** node distribution; **b** element distribution

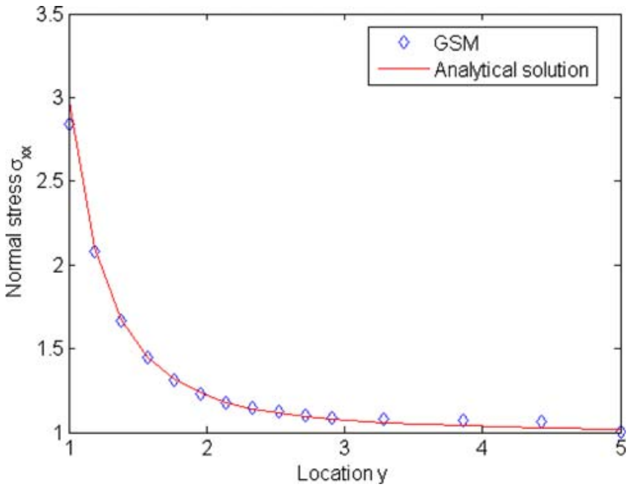

Fig. 18 Normal stress σ_{xx} along the edge of $x = 0$ in a plate with a central hole subjected to a unidirectional tensile load

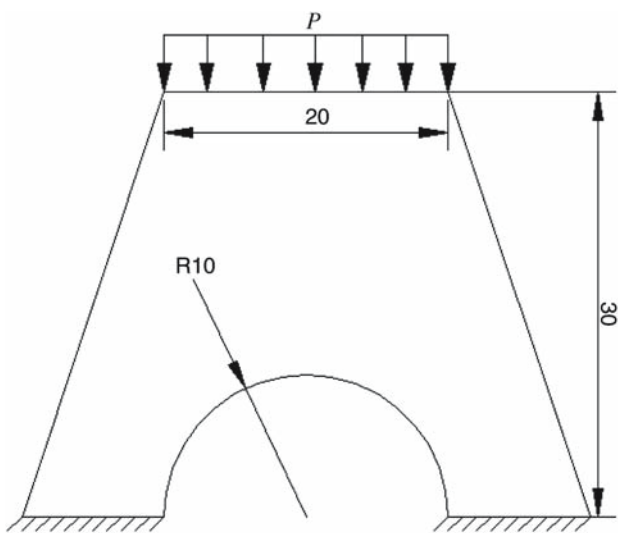

Fig. 19 A bridge pier subjected to a uniformly distributed pressure on the top

than discontinue like the FEM. Also, the shear stress τ_{xy} plotted in Fig. 15 is more accurate than that of FEM. From this point of view, the GSM does perform better than the FEM for computing the stresses.

Table 5 shows the comparison of the computational efficiency between GSM and FEM using the same set of meshes of 273, 527, 1,127, 2,275 and 3,825 regularly distributed nodes. It is found that GSM uses less CPU time than FEM when a small number of nodes are used. This is because of that when node number is small the CPU time is largely controlled by the overhead operations in creating the algebraic system equations. As GSM creates the system equations by discretizing directly (by collocation) the governing equation and does not need any integration that is on the other hand necessary for FEM, the GSM is therefore more efficient than FEM when a small number of nodes are used. This is clearly demonstrated in Table 5. When a large number of nodes are used, however, the CPU time is mainly determined by solving the algebraic system equations. In this case FEM is faster than GSM, but is only about twice faster. This can be examined simply by the complicity analysis of the equation solvers used in the FEM and GSM. We know that the bandwidth of the system matrix generated by GSM is the same as the FEM, but the matrix in GSM is not symmetric and a solver for asymmetric system equations needs to be used. In the FEM, however, the matrix is symmetric and hence a solver for symmetric system equations can be used. The complexity of a symmetric solver is about twice faster than an asymmetric solver for matrices of the same dimension and bandwidth. This analysis is confirmed numerically as shown in Table 5.

Our conclusion is: (1) for small systems, GSM is more efficient than FEM, and gives more accurate results in terms of stresses; (2) for large systems, FEM is about twice as faster as GSM, but GSM gives more accurate results in terms of stresses.

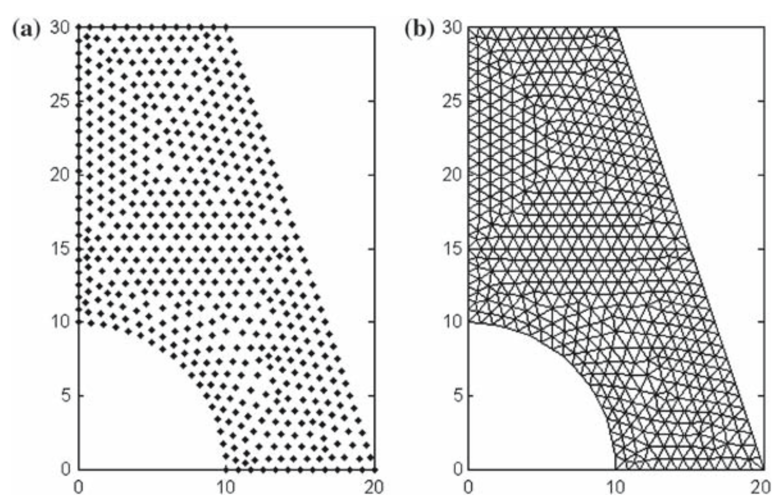

Fig. 20 Half model of the bridge pier: **a** node distribution; **b** element distribution

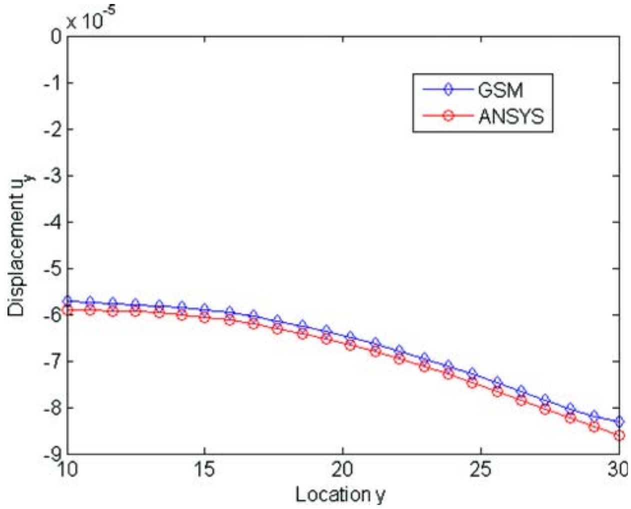

Fig. 21 Displacement in y-direction along the line $x = 0$ (GSM uses 1,077 triangular elements while ANSYS adopts a very fine triangular mesh to get the reference solution)

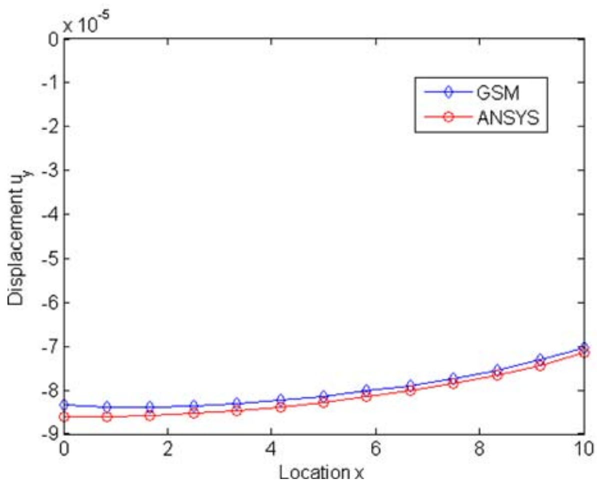

Fig. 22 Displacement in y-direction along the line $y = 30$ (GSM uses 1,077 triangular elements while ANSYS adopts a very fine triangular mesh to get the reference solution)

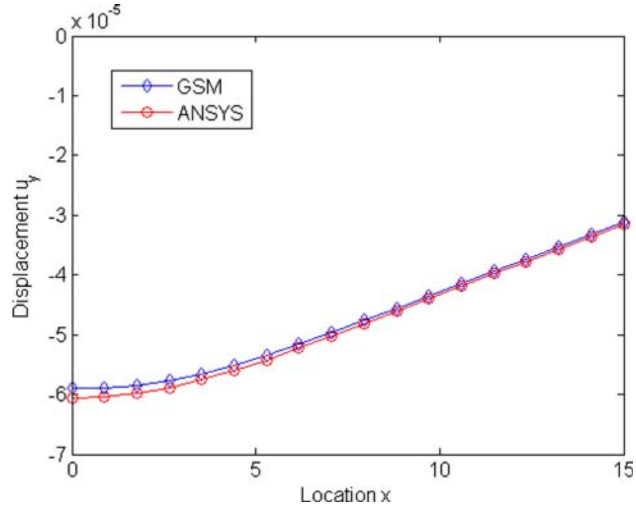

Fig. 23 Displacement in y-direction along the line $y = 15$ (GSM uses 1,077 triangular elements while ANSYS adopts a very fine triangular mesh to get the reference solution)

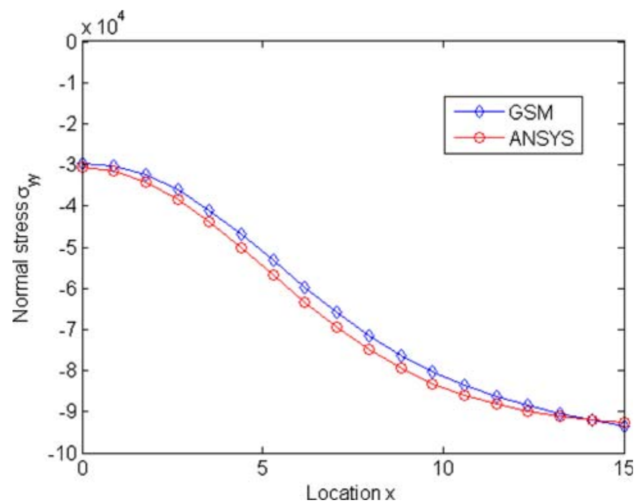

Fig. 24 Normal stress σ_{yy} along the line $y = 15$ (GSM uses 1,077 triangular elements while ANSYS adopts a very fine triangular mesh to get the reference solution)

4.2 Infinite plate with a circular hole

To validate the GSM in simulating stress concentration, we consider an infinite plate with a central circular hole subjected to a unidirectional tensile load $p = 1.0$ in the x-direction. Due to the symmetry, only the upper right quadrant of the plate is modelled, as shown in Fig. 16, in which the plane strain problem is considered, and the geometries and material parameters used are $a = 1, b = 5$, Young's modulus $E = 1.0 \times 10^3$ and Poisson's ratio $\nu = 0.3$. Symmetry conditions are imposed on the left and bottom edges, and the inner boundary of the hole is traction free. The corresponding exact solutions for the stresses in the plate are given in the polar coordinate [41]:

$$\sigma_{xx} = 1 - \frac{a^2}{r^2}\left(\frac{3}{2}\cos 2\theta + \cos 4\theta\right) + \frac{3}{2}\frac{a^4}{r^4}\cos 4\theta \tag{49}$$

$$\sigma_{xy} = -\frac{a^2}{r^2}\left(\frac{1}{2}\sin 2\theta + \sin 4\theta\right) + \frac{3}{2}\frac{a^4}{r^4}\sin 4\theta \tag{50}$$

$$\sigma_{yy} = -\frac{a^2}{r^2}\left(\frac{1}{2}\cos 2\theta - \cos 4\theta\right) - \frac{3}{2}\frac{a^4}{r^4}\cos 4\theta \tag{51}$$

where (r, θ) are the polar coordinates and θ is measured counterclockwise from the positive x-axis. The traction boundary conditions given by the exact solutions (49)–(51) are imposed on the right ($x = 5$) and top ($y = 5$) edges.

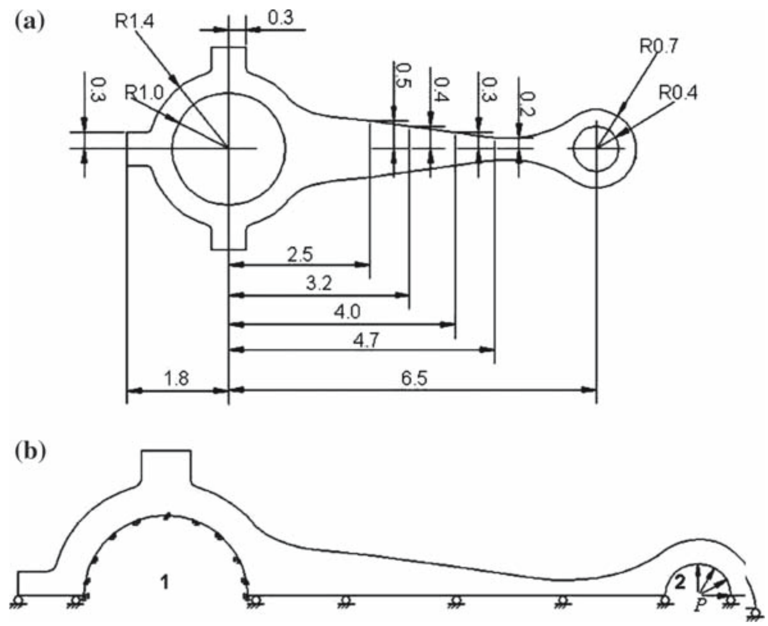

Fig. 25 An automotive part: the connecting rod

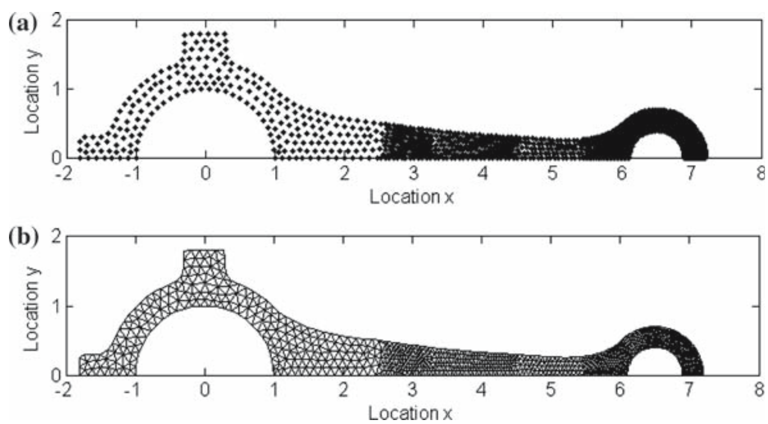

Fig. 26 Half model of the connecting rod: **a** node distribution; **b** element distribution

Figure 17a shows the distribution of 261 irregular nodes in the problem domain, in which there are 465 triangular elements (see Fig. 17b). The distribution of normal stress σ_{xx} along the line $x = 0$ obtained using the GSM is shown in Fig. 18. It can be observed from this figure that the GSM yields very satisfactory results for the stress concentration problem.

4.3 Bridge pier

In this example, the GSM is used for the stress analysis of a bridge pier subjected to a uniformly distributed pressure on the top, as shown in Fig. 19. The problem is solved as a plain strain case with material properties $E = 4 \times 10^{10}$ Pa, $\upsilon = 0.15$ and loading $P = 10^5$ Pa.

Due to the symmetry, only right half of the bridge is modelled as shown in Fig. 20 where there are 590 field nodes (see Fig. 20a) in the model and 1,077 triangular elements (see Fig. 20b). As there are no analytical solutions available for this problem, a reference solution of displacements and stresses are computed with commercial software ANSYS using very fine triangular mesh for purpose of validation.

The displacements in y-direction along the lines $x = 0$, $y = 30$ and $y = 15$ are plotted in Figs. 21, 22 and 23, respectively. The solutions obtained by GSM are in good agreement with the reference (ANSYS) solutions. Also, comparison of the stress distribution σ_{yy} along the line $y = 15$ computed by the GSM and ANSYS is shown in Fig. 24. It can be concluded from the figure that the GSM results are accurate enough for general engineering requirement.

4.4 An automotive part: connecting rod

As the last numerical example, to generalize the present GSM to all problem domains with irregular shapes, a connecting rod as an automotive part with complicated geometry is

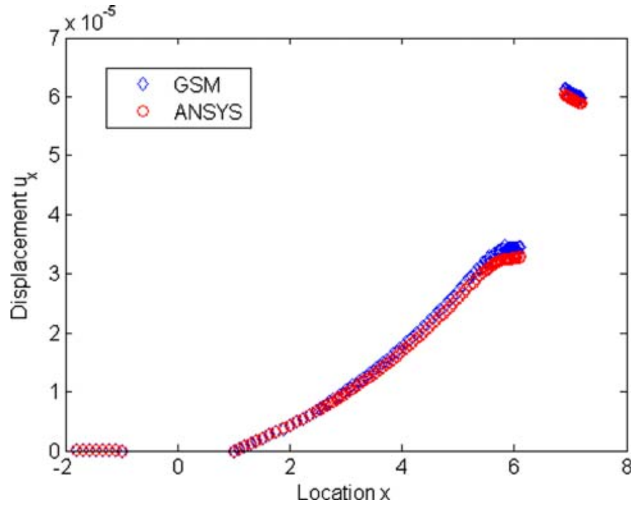

Fig. 27 Displacement in X-direction along the line $y = 0$ (GSM uses 2,877 triangular elements while ANSYS adopts a very fine triangular mesh to get the reference solution)

studied as a plane stress solid mechanics problem, as shown in Fig. 25a. The material properties are given as Young's modulus $E = 3 \times 10^7$ Pa and Poisson's ratio $\upsilon = 0.3$. The edge of the hole **1** is fixed and the right edge of the hole **2** is subjected to a constant pressure $P = 200$ Pa (see Fig. 25b). Due to symmetry, only upper half of the connecting rod is simulated and shown in Fig. 25b. Symmetric conditions are imposed along the bottom edge of the half connecting rod.

Figure 26a shows the node distribution of 1,634 irregular field nodes, in which there are 2,877 triangular elements in the problem domain, as shown in Fig. 26b. Since no analytical solution is available for this problem, commercial FEM software, ANSYS, is also used to compute the reference solutions with a very fine mesh of triangular elements for purpose of comparison.

Figure 27 shows the displacement in x-direction along the line $y = 0$. The stress distributions σ_{xx} and σ_{yy} along the line $y = 0$ by GSM are plotted in Fig. 28a and b. It can be found that the GSM results are very accurate compared with the ANSYS reference solutions.

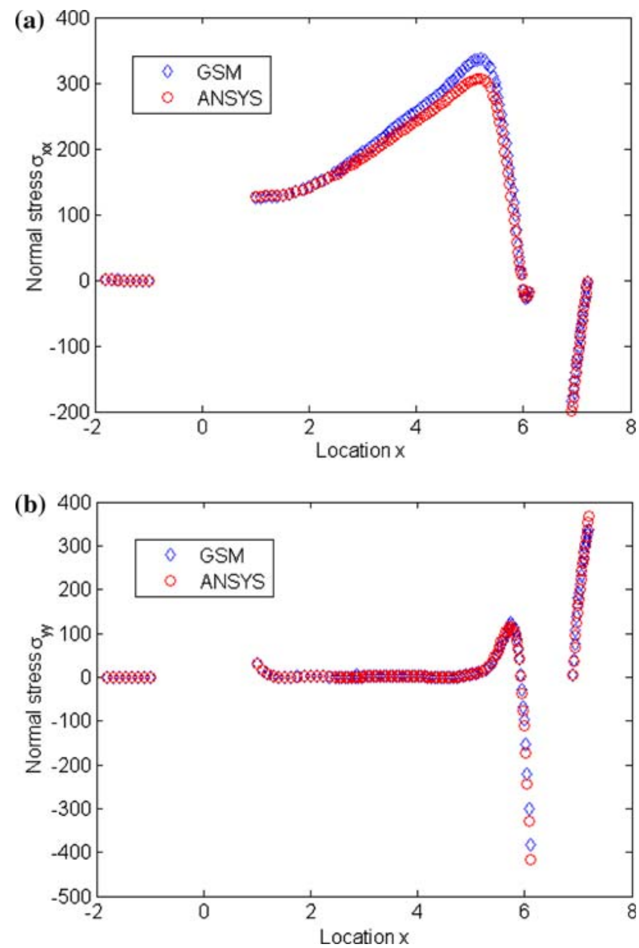

Fig. 28 Distribution of normal stresses along the line $y = 0$: **a** σ_{xx}; **b** σ_{yy} (GSM uses 2,877 triangular elements while ANSYS adopts a very fine triangular mesh to get the reference solution)

5 Conclusions

In this paper, a gradient smoothing method (GSM) has been presented for solving partial differential equations, with emphases on solid mechanics problems. By adopting the gradient smoothing together with the directional derivative correction, the first- and second-order derivative approximations can be obtained with a favourable weight distribution for a set of field nodes surrounding the interest node. Unlike the traditional finite difference method with structured and orthogonal grids or the generalized finite difference methods with some topological requirements, the GSM is flexible to perform the use of pre-existing meshes which are originally created for finite element or finite difference methods, regardless of their topology. The selected star of the GSM is simply generated by sequentially connecting the centroids with mid-edge points of surrounding elements for the interested node, compared with the Voronoi neighborhood criterion. Since the GSM directly discretizes the governing equations using the gradient smoothing technique, the first-order continuity can be obtained which leads to the better results in the computations of stresses and strains for solid mechanics problems compared with the finite element method. By comparison with FEM (ANSYS) or analytical solution via several numerical examples, it can be concluded that the proposed method achieves very accurate and stable solutions using arbitrary and irregular computational meshes.

Compared with the FEM, GSM is more efficient than FEM, and gives more accurate results in terms of stresses when a small number of nodes are used. For large systems, FEM is about twice as faster as GSM, but GSM give more accurate results in terms of stresses.

The method can be easily applied to adaptive analysis and three-dimensional problems.

References

1. Richtmyer RD (1957) Difference methods for initial-value problems. Wiley, New York
2. Forsythe GE, Wasow WR (1960) Finite difference methods for partial differential equations. Wiley, New York
3. Richtmyer RD, Morton KW (1967) Difference methods for boundary-value problems. Wiley, New York
4. Samarskij AA (1977) Theory of finite difference schemes (in Russian). Nauka, Moscow
5. Gawain TH, Ball RE (1978) Improved finite difference formulas for boundary-value problems. Int J Num Meth Eng 12:1151–1160
6. Anderson DA, Tannenhill JC, Fletcher RH (1984) Computational fluid mechanics and heat transfer. McGraw-Hill, Washington
7. Frey WH (1977) Flexible finite-difference stencils from isoparametric finite elements. Int J Numer Methods Eng 11:1653–1665
8. Lau PC (1979) Curvilinear finite difference method for biharmonic equation. Int J Numer Methods Eng 14:791–812
9. Lau PC (1979) Curvilinear finite difference methods for three-dimensional potential problems. J Comput Phys 32:325–344
10. Kwok SK (1984) An improved curvilinear finite difference (CFD) method for arbitrary mesh systems. Comput Struct 18:719–731
11. Nay RA, Utku S (1973) An alternative for the finite element method. Variat Mech Eng 3:62–74
12. Wyatt MJ, Davies G, Snell C (1975) A new difference based finite element method. Instn Eng 59:395–409
13. Mullord P (1979) A general mesh finite difference method using combined nodal and element interpolation. Appl Math Modell 3:433–440
14. Snell C, Vesey DG, Mullord P (1981) The application of a general finite difference method to some boundary value problems. Comput Struct 13:547–552
15. Tworzydlo W (1987) Analysis of large deformation of membrane shells by the generalized finite difference method. Comput Struct 27:39–59
16. Liu GR (2003) Meshfree method: moving beyond the finite element method. CRC Press, Boca Raton
17. Liu GR, Gu YT (2005) An introduction to meshfree methods and their programming. Springer, Dordrecht
18. Belytschko T, Krongauz Y, Organ D, Fleming M, Krysl P (1996) Meshless methods: an overview and recent developments. Comput Methods Appl Mech Eng 139:3–47
19. Liu GR, Gu YT (2001) A point interpolation method for two-dimensional solids. Int J Numer Methods Eng 50:937–951
20. Liu GR, Gu YT (2001) A local point interpolation method (LRPIM) for free vibration analyses of 2-D solids. J Sound Vib 246:29–46
21. Gu YT, Liu GR (2005) A Meshfree Weak-Strong (MWS) form method for time dependent problems. Comput Mech 35:134–145
22. Liu GR, Zhang Jian, Li Hua, Lam KY, Kee BT Bernard (2006) Radial point interpolation based finite difference method for mechanics problems. Int J Numer Methods Eng 68:728–754
23. Jensen PS (1972) Finite difference techniques for variable grids. Comput Struct 2:17–29
24. Perrone N, Kao R (1975) A general finite difference method for arbitrary meshes. Comput Struct 5:45–58
25. Krok J, Orkisz J (1990) A unified approach to the FE generalized variational FD method in nonlinear mechanics: concept and numerical approach. In: Discretization methods in structural mechanics. Springer, Berlin, pp 353–362
26. Krok J, Orkisz J, Stanuszek M (1993) A unique FDM/FEM system of discrete analysis of boundary value problems in mechanics. In: Proceedings of the 11th Polish conference on computational methods in mechanics. Kielce-Cedzyna, Poland, pp 466–472
27. Krok J, Orkisz J (1997) 3D elastic stress analysis in railroad rails and vehicle wheels by the adaptive FEM/FDM and Fourier series. In: Proceedings of the 13th Polish conference on computational methods in mechanics. Poznan, Poland, pp 661–668
28. Orkisz J (1997) Adaptive approach to the finite difference method for arbitrary irregular grids. In: Interdisciplinary symposium on advances in computational mechanics. University of Texas, Austin
29. Orkisz J, Lezanski P, Przybylski P (1997) Multigrid approach to adaptive analysis of boundary-value problems by the meshless GFDM. In: IUTAM/IACM symposium on discretization methods in structural mechanics II. Vienna
30. Liszka T, Orkisz J (1980) The finite difference method at arbitrary irregular grids and its application in applied mechanics. Comput Struct 11:83–95
31. Liszka T (1984) An interpolation method for an irregular net of nodes. Int J Numer Methods Eng 20:1599–1612
32. Orkisz J (1998) Meshless finite difference method I: Basic approach. In: Proceedings of the IACM-fourth world congress in computational mechanics, Argentina
33. Kleiber M (ed) (1998) Handbook of computational solid mechanics: survey and comparison of contemporary methods. Springer, Berlin
34. Chen JS, Wu CT, Yoon S, You Y (2001) A stabilized conforming nodal integration for Galerkin mesh-free methods. Int J Numer Methods Eng 50:435–466
35. Liu GR, Li Y, Dai KY, Luan MT, Xue W (2006) A linearly conforming RPIM for 2D solid mechanics. Int J Comput Methods (in press)
36. Liu GR, Dai KY, Nguyen TT (2007) A smoothed finite element method for mechanics problems. Comput Mech 39:859–877
37. Shepard D (1968) A two dimensional interpolation function for irregularly spaced points. In: Proceeding of ACM national conference, pp 517–524
38. Haselbacher A, Blazek J (2000) Accurate and efficient discretization of Navier–Stokes equations on mixed grids. AIAA J 38:2094–2102
39. Weiss JM, Maruszewski JP, Smith WA (1999) Implicit solution of preconditioned Navier-Stokes equations using algebraic multigrid. AIAA J 37:29–36
40. Blazek J (2001) Computational fluid dynamics: principles and applications, 1st edn. Elsevier, Oxford
41. Timoshenko SP, Goodier JN (1970) Theory of elasticity, 3rd edn. McGraw-Hill, New York